LETTER

https://doi.org/10.1038/s41586-019-0976-y

Observation of moiré excitons in WSe_2/WS_2 heterostructure superlattices

Chenhao Jin[1,9], Emma C. Regan[1,2,9], Aiming Yan[1,3], M. Iqbal Bakti Utama[1,4], Danqing Wang[1,2], Sihan Zhao[1], Ying Qin[5], Sijie Yang[5], Zhiren Zheng[1], Shenyang Shi[1,6], Kenji Watanabe[7], Takashi Taniguchi[7], Sefaattin Tongay[5], Alex Zettl[1,3,8] & Feng Wang[1,3,8]*

[1]Department of Physics, University of California at Berkeley, Berkeley, CA, USA. [2]Graduate Group in Applied Science and Technology, University of California at Berkeley, Berkeley, CA, USA. [3]Material Science Division, Lawrence Berkeley National Laboratory, Berkeley, CA, USA. [4]Department of Materials Science and Engineering, University of California at Berkeley, Berkeley, CA, USA. [5]School for Engineering of Matter, Transport and Energy, Arizona State University, Tempe, AZ, USA. [6]Department of Physics, Fudan University, Shanghai, China. [7]National Institute for Materials Science, Tsukuba, Japan. [8]Kavli Energy NanoSciences Institute at University of California Berkeley and Lawrence Berkeley National Laboratory, Berkeley, CA, USA. [9]These authors contributed equally: Chenhao Jin, Emma C. Regan. *e-mail: fengwang76@berkeley.edu

Supplementary Materials for

Observation of Moiré Excitons in WSe_2/WS_2 Heterostructure Superlattices

Chenhao Jin†, Emma C. Regan†, Aiming Yan, M. Iqbal Bakti Utama, Danqing Wang, Sihan Zhao, Ying Qin, Sijie Yang, Zhiren Zheng, Shenyang Shi, Kenji Watanabe, Takashi Taniguchi, Sefaattin Tongay, Alex Zettl, Feng Wang*

† These authors contributed equally to this work

* Correspondence to: fengwang76@berkeley.edu

1. Determination of the relative twist angle between WSe_2 and WS_2 layers

The crystal orientation of WSe_2 and WS_2 flakes can be obtained from the second harmonic generation (SHG) polarization dependence with an uncertainty of ~ 0.3 degree.

Since the SHG patterns of both materials have six-fold rotational symmetry, the case of AA stacking (~ 0 twist angle) and AB stacking (~ 60 twist angle) cannot be differentiated by separately measuring the SHG of each material. On the other hand, the two cases can be distinguished by directly measuring the SHG of the heterostructure: in AA (AB) stacking case, the second harmonic field of the two layers will constructively (destructively) interfere, giving SHG signal stronger (weaker) than monolayers. Figure S1 shows the SHG intensity from WSe_2 alone, WS_2 alone, and heterostructure regions in device D1 measured with a 900 nm incident beam and the same experimental configuration. The WSe_2 and WS_2 regions show similar SHG intensity, while the heterostructure region show SHG intensity approximately four times larger than the monolayer. This result indicates that the twist angle between WSe_2 and WS_2 layers is near zero, i.e. AA-stacking.

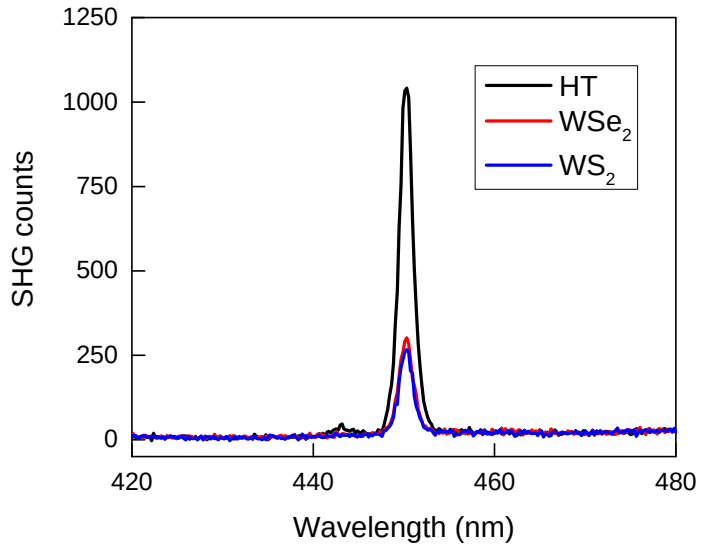

Fig. S1. SHG signal of device D1 measured on the WSe_2 alone (red), WS_2 alone (blue), and heterostructure (black) regions with the same experimental configuration.

2. Determination of the moiré periodicity

The periodicity of the moiré superlattice in WSe_2/WS_2 heterostructures is given by

$$L_M \approx a/\sqrt{\delta^2 + \theta^2},$$

where a is the lattice constant of WSe_2, and δ and θ are the relative lattice constant difference and the twist angle between the two layers, respectively. WSe_2 and WS_2 layers have a large lattice constant mismatch of ~ 4%. As a result, the moiré periodicity is mainly determined by the intrinsic lattice constant mismatch and is not significantly affected by a small angular mismatch. For example, if the interlayer twist angle changes from 0 to $\pm 0.5°$, the moiré periodicity will change from 8 nm to ~7.8 nm.

3. Subtraction of background in reflection contrast spectra

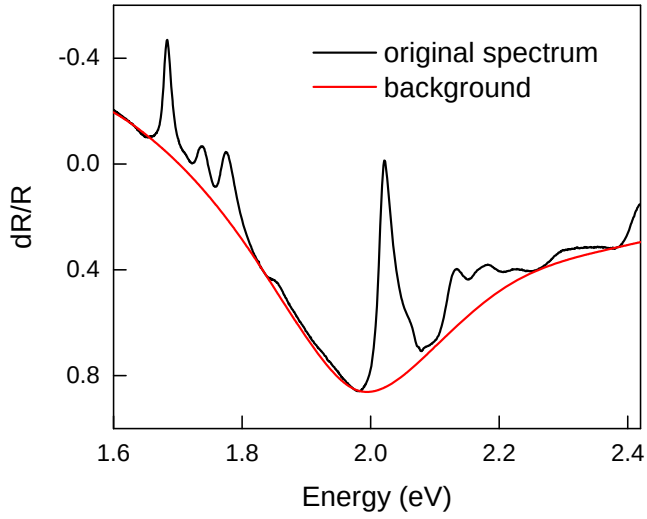

Fig. S2. Original reflection contrast (black) and the slow-varying background (red) obtained from polynomial fitting.

The WSe_2/WS_2 heterostructure is encapsulated in two pieces of hBN and placed on 90 nm SiO_2/Si substrate. This multi-film structure introduces interference between reflections at different interfaces, leading to a background signal from the real part of the dielectric function of the heterostructure[32], see Fig. S2. Because the phase difference between the multi-reflections in the interference depend on the light wavelength, this background signal will vary with photon energy. To better resolve the exciton absorption resonances (i.e. the imaginary part of dielectric function), we obtain a slowly-varying background signal through polynomial fitting of the spectra using regions away from resonances (red curve in Fig. S2). The same background is used universally to obtain background-subtracted spectra at charge neutral (Fig. 2 in text) and at different doping levels (Fig. 3 in text).

To further demonstrate the validity of the absorption spectra obtained through background subtraction, we performed a numerical simulation of the reflection contrast from the device, as shown in Fig. S3a. The simulated reflection contrast (red) is compared to the experimentally measured one (blue); and the extracted real (blue) and imaginary (red) part of the system's dielectric function is shown in Fig. S3b. This comparison confirms that for the layer structure in our experimental configuration, the local field effect mainly creates a broad interference background, and the profiles of the absorption peaks are only slightly modified in the energy range of interest.

In addition, the spectral profile in PLE spectroscopy is simpler and background-free because it is not affected by the real part of the dielectric function. As shown in Fig. 2c, the spectra from the reflection contrast results after the background subtraction match very well with the spectra from the PLE measurement. This provides another independent confirmation of the validity of our analysis on the reflection contrast spectra.

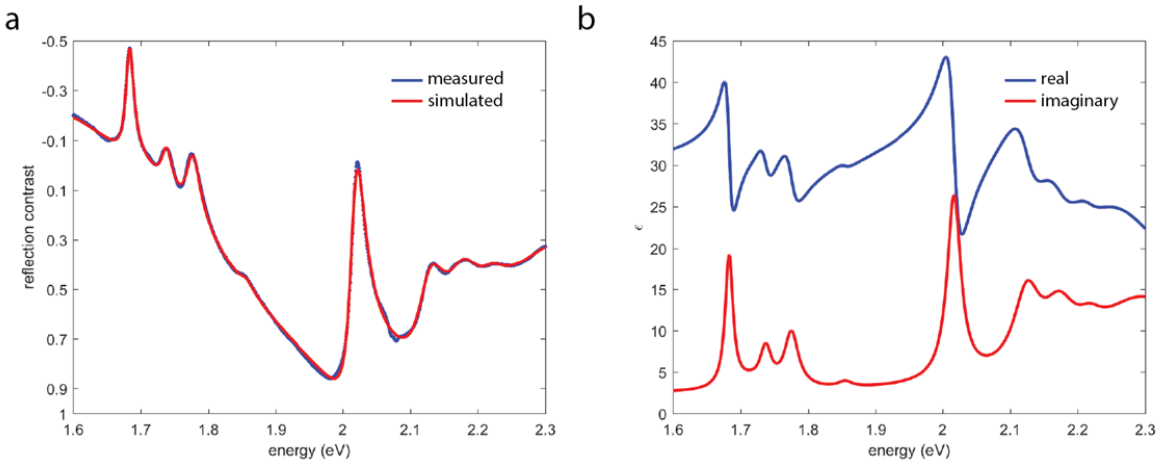

Fig. S3 **a**, Comparison between simulated reflection contrast in the experimental device configuration (red) and the measured results (blue). **b**, Extracted real (blue) and imaginary (red) part of the heterostructure's dielectric function.

4. Results from additional near-aligned heterostructures

The moiré excitons observed in device D1 and described in the text are reproducible in all near-aligned heterostructures that we fabricated, with crystals from several commercial and academic sources. For example, Fig. S4 shows the reflection contrast and PLE measurement results from another near-aligned heterostructure device D3 when it is slightly n-doped. Four resonances (I', I, II, III) are clearly observed between 1.6 and 1.9 eV in both reflection contrast and PLE spectra,

whose energy and amplitude match well with the corresponding resonances observed for device D1.

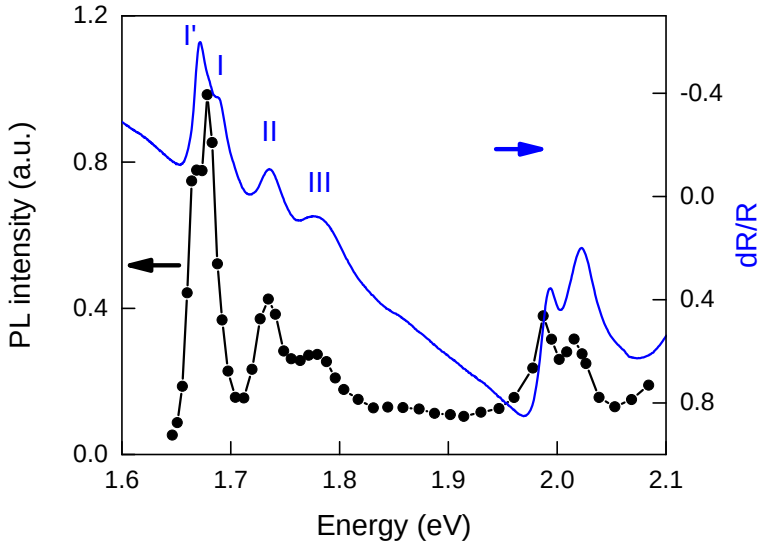

Fig. S4. Reflection contrast (blue) and PLE (black) spectra of another near-aligned heterostructure D3 at slight n-doping.

5. Twist-angle dependence of reflection contrast spectra

We systematically investigate the twist-angle dependence of the moiré superlattice excitons by measuring 18 different WSe_2/WS_2 heterostructures (including device D1 and D3) spanning a large range of twist angles. The reflection contrast spectra for the 18 devices are displayed in Fig. S5. The twist angle in each of the device is determined by the polarization-dependent second harmonic generation measurements with an uncertainty of ~ 0.3 degree.

Overall, the spectra can be classified into three groups. For WSe_2/WS_2 heterostructures with twist angle < 1 degree, the spectra consistently show three prominent absorption peaks from moiré exciton states. The variation of the broad background is due to the different local field factor between devices. If the twist angle is large (>3 degree), the spectra largely recovers to the response of weakly-coupled bilayers, where only a single prominent peak is present in the range of WSe_2 A exciton. For twist angles between 1 and 3 degree, the spectra show intermediate behaviors: the higher energy side peaks from the moiré superlattice are very weak and barely observable, and the lowest energy (and most prominent) exciton peak has a resonance energy between the near-zero twisting angle and large twist angle samples.

Moiré superlattices with a large moiré period also exist for WSe_2/WS_2 heterostructures with twist angle near 60 degree (AB stacking). We show in Fig. S5 the twist-angle-dependent absorption spectra of heterostructures close to AB stacking, which exhibits behavior similar to the case of near-AA stacking: The moiré excitons are clearly present at <1 degree twist angle and disappear completely at >3 degree twist angle.

One representative signature of the moiré superlattice is its effect on the lowest-energy exciton peak position, which can be clearly observed in all twist angles. We summarize in Fig. S6 the twist angle-dependence of the lowest-energy exciton peak position. Black and red symbols represent results from near-AA stacked and near-AB stacked bilayers, respectively. Three large-twist-angle (>10 degree) devices are also included as reference (grey symbols). As one can see clearly, at small twist angle (<1 degree), the lowest-energy exciton peaks show a systematic redshift of ~40 meV, which is due to the moiré potential discussed in the text (see Fig. 4c). As the twist angle increases, this redshift quickly goes away and completely disappears at > 3 degree, consistent with the range in which the moiré exciton peaks vanishes. The abrupt disappearance of the moiré exciton peaks, as well as the energy redshift, can be potentially understood from the fact that a large lattice corrugation may be formed at near-zero twist angle[21,22], which becomes increasingly unstable at larger twist angle and undergoes a sudden relaxation at some critical angle. Because the amplitude of the moiré potential depends sensitively on the lattice corrugation, a sudden change of the latter can cause a large change in the moiré potential and its effect on the excitons.

Twist angle: <1 degree from AA stacking

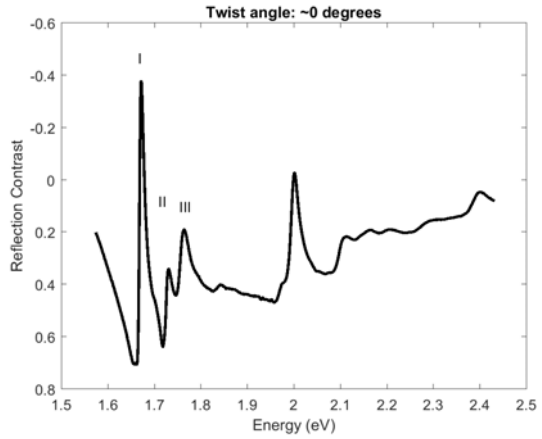

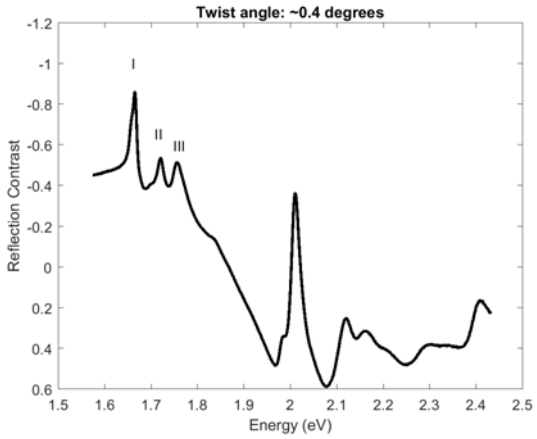

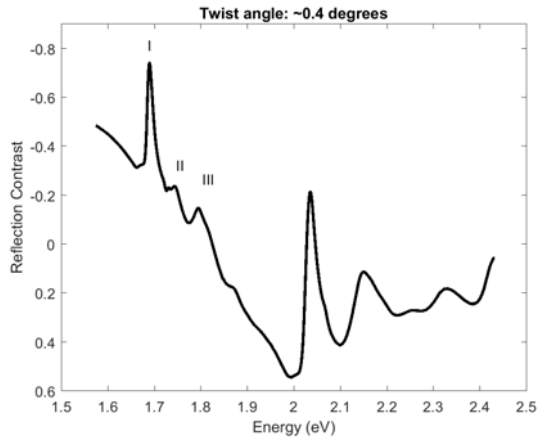

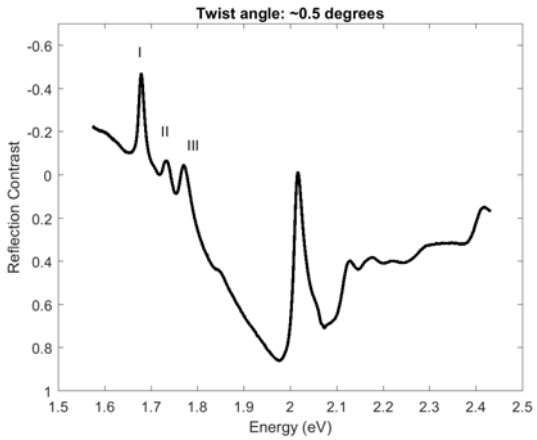

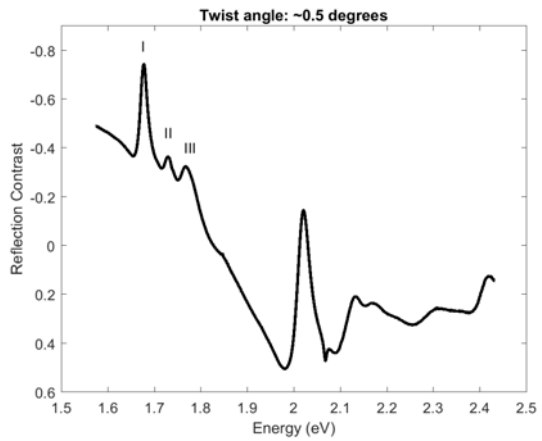

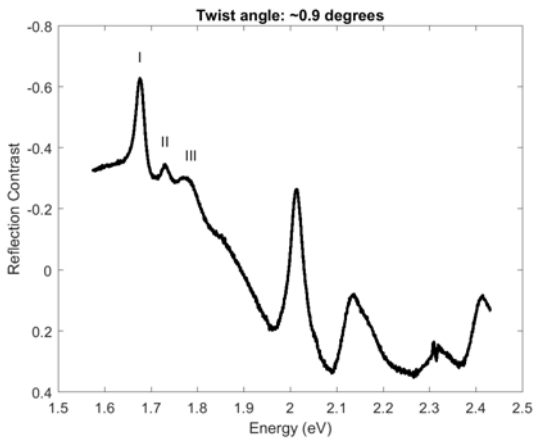

Twist angle: 1-3 degrees from AA stacking

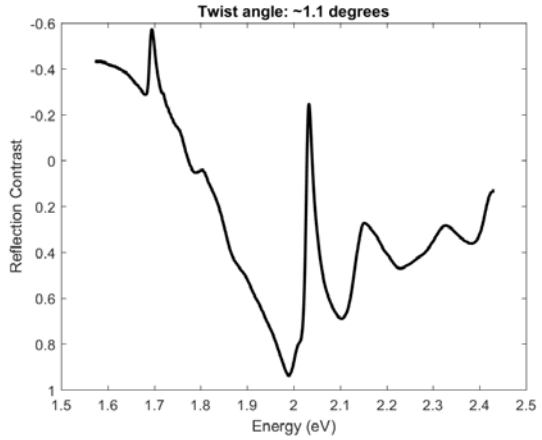

Twist angle: >3 degrees from AA stacking

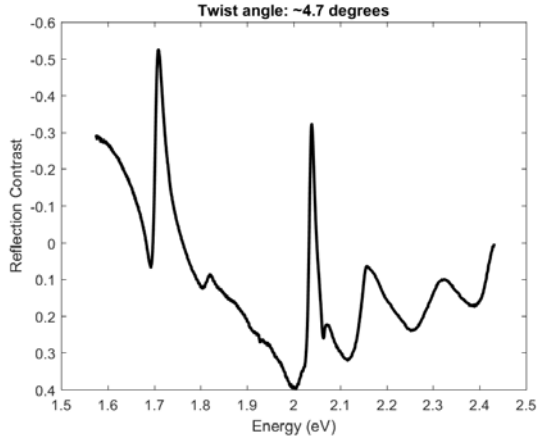

Twist angle: <1 degree from AB stacking

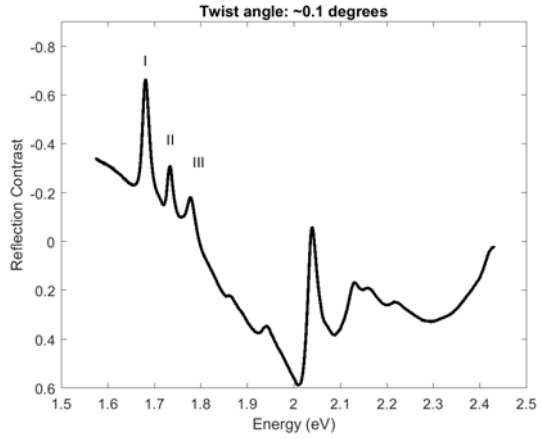

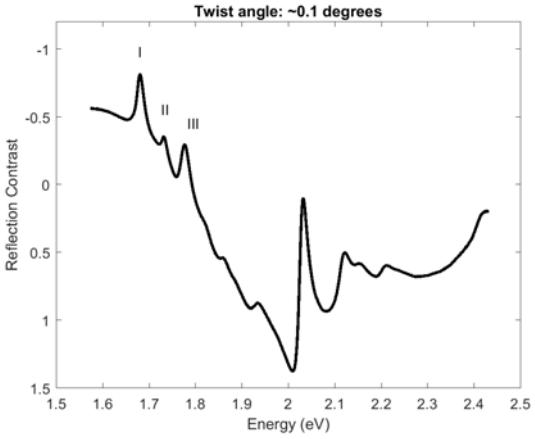

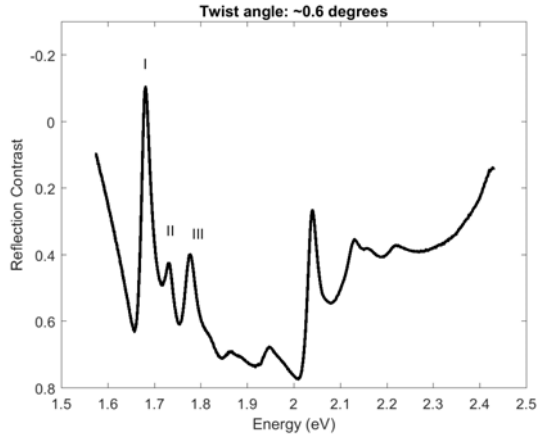

Twist angle: 1-3 degrees from AB stacking

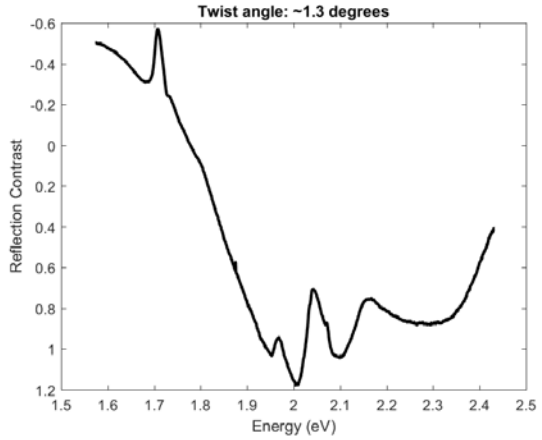

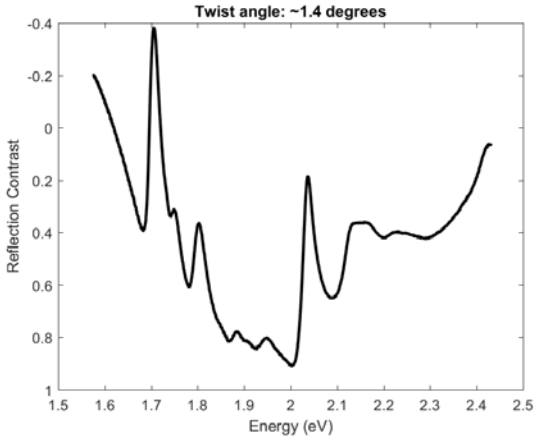

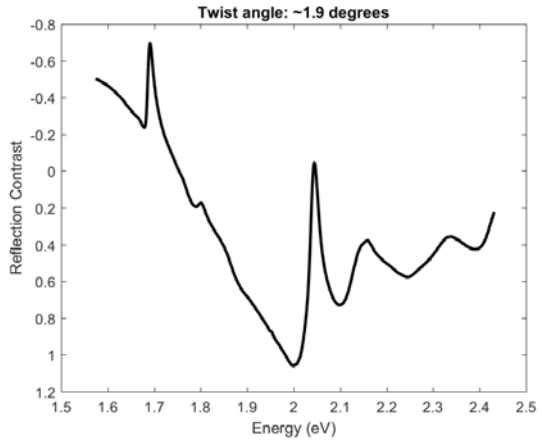

Twist angle: >3 degrees from AB stacking

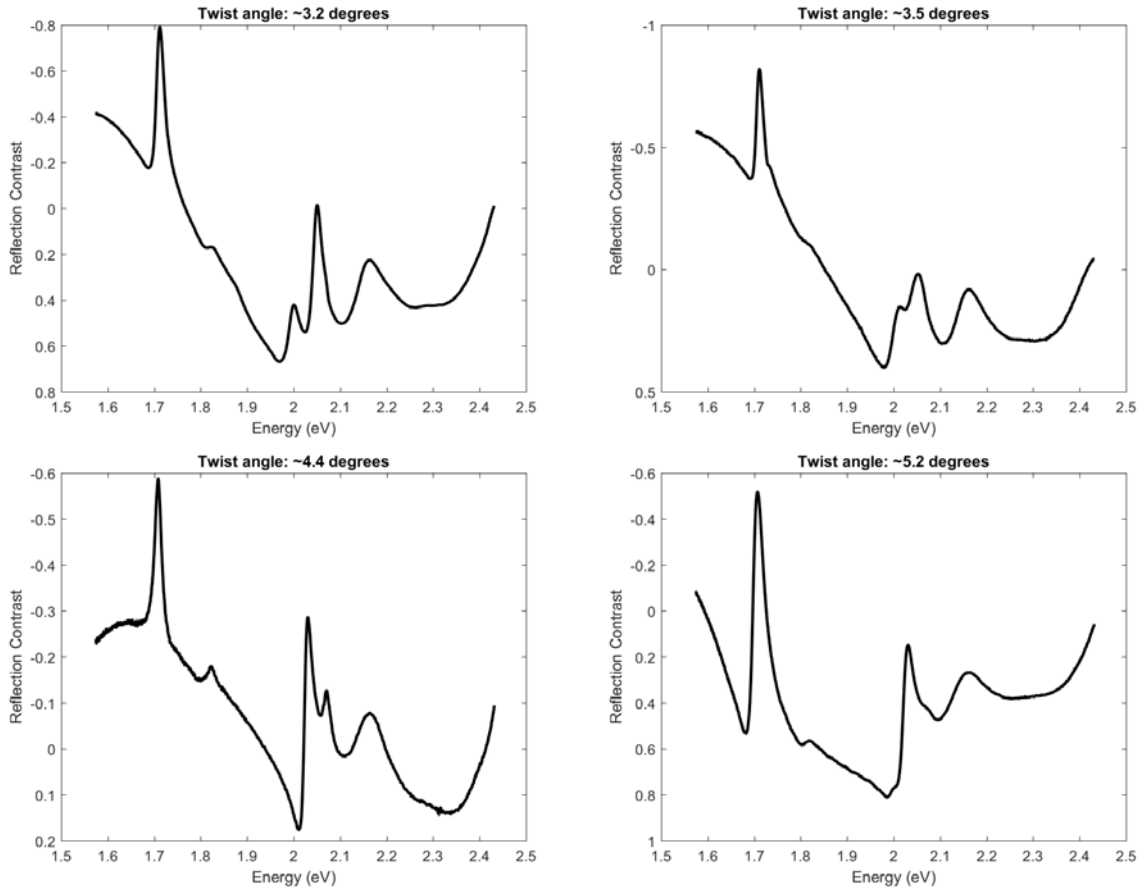

Fig. S5. Reflection-contrast spectra from 18 WSe_2/WS_2 heterostructures spanning a large range of twist angles. Moiré exciton peaks I, II, and III are labelled for devices with twist angle < 1 degree from AA and AB stacking.

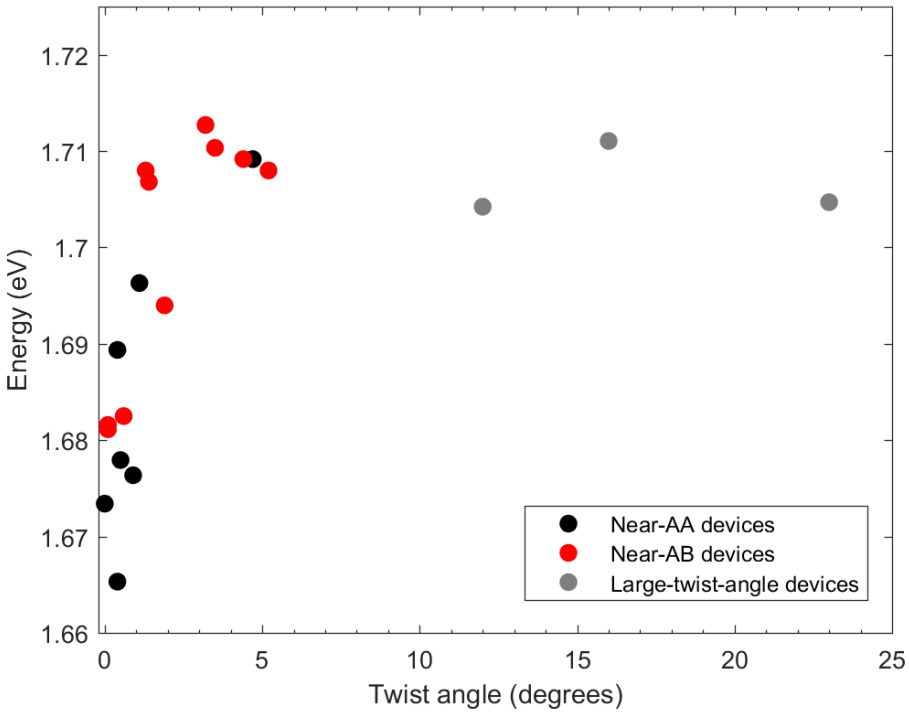

Fig. S6. Twist-angle-dependence of the lowest-energy exciton peak position. Black and red symbols represent results from near-AA stacked and near-AB stacked bilayers, respectively. Three large-twist-angle (>10 degree) devices are also included as reference (grey symbols).

6. Comparison of doping-dependent absorption between large-twist-angle and near-aligned WSe_2/WS_2 heterostructure

The strong influence of the moiré potential on the doping-dependent absorption can be directly seen by comparing the spectra of near-aligned WSe_2/WS_2 heterostructures to the spectra of large-twist-angle WSe_2/WS_2 heterostructures. As shown in Fig. S7, with electron doping (positive carrier concentration), the WSe_2 A exciton almost does not change at all in large-twist-angle heterostructures. This behavior originates from the type II band alignment of the WSe_2/WS_2 heterostructures: Both the conduction and valance bands of WSe_2 are higher than those of WS_2. As a result, electrons stay in the WS_2 layer when the whole system is electron-doped, and the optical response from WSe_2 largely remains unchanged. The dramatic change of the WSe_2 moiré exciton peaks with electron-doping in the near-aligned WSe_2/WS_2 heterostructures is therefore

quite surprising, which indicates that the interlayer electron-exciton interaction is strongly enhanced through the moiré superlattice.

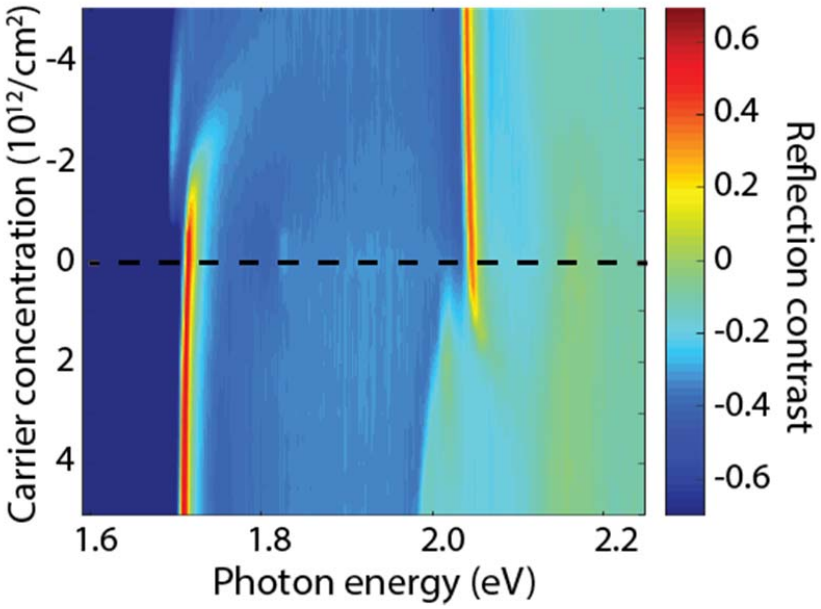

Fig. S7 Representative doping-dependent reflection contrast in large-twist-angle WSe_2/WS_2 heterostructure. Positive and negative carrier concentration correspond to electron- and hole-doping, respectively. This plot is reproduced from Ref. 33.

The observed gate dependence of moiré excitons can be qualitatively understood from the model provided in the manuscript. Because of the different wavefunction distributions, peak II is not strongly affected by electron-doping the system, while exciton states I and III can interact strongly with electrons. In monolayer WSe_2, the interaction between excitons and electrons leads to the emergence of the trion peaks and a blueshift of the exciton peaks in the absorption spectrum. Through this analogy, we can qualitatively understand the gate-dependences of peak I and III as blue-shifted exciton peaks due to electron doping, and the peak I' as an interlayer trion state in the moiré superlattice.

On the other hand, a full picture to quantitatively determine the doping-dependence of the moiré exciton states is quite complicated. Several important elements need be added into the model, including lattice relaxation and corrugation, interlayer electronic states hybridization, and many-body interaction (e.g. regarding the formation and binding energy of trion state). Further theoretical and experimental work is therefore required for a quantitative description of this non-trivial doping dependence.

7. Temperature dependent reflection contrast spectra in near-aligned heterostructures

Fig. S8 shows the reflection contrast spectra of a nearly-aligned WSe_2/WS_2 heterostructure at several elevated temperature. We find that the moiré exciton peaks largely remain the same from 10 to 100 K, except for relatively weak broadening and redshift at higher temperatures. This is expected because the moiré potential in the heterostructure is orders of magnitude larger than the thermal energy in this temperature range.

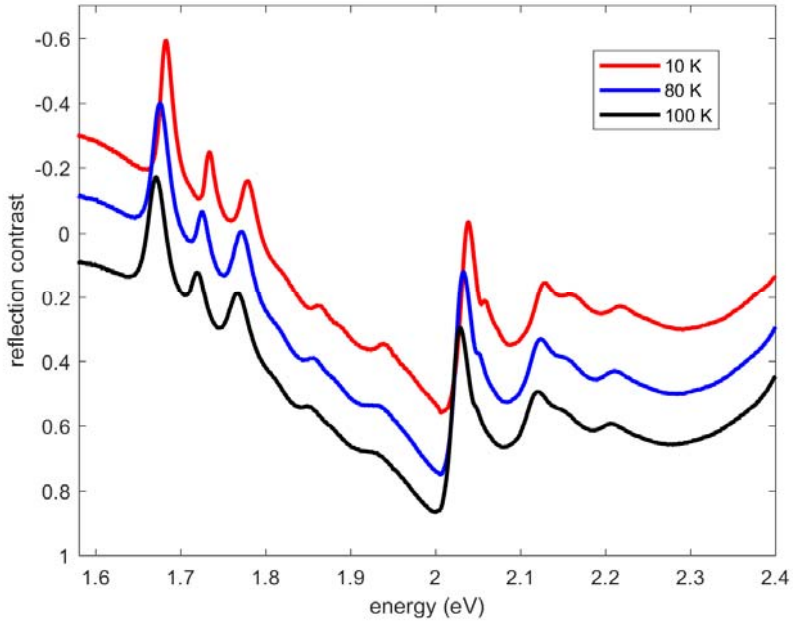

Fig. S8 Representative temperature-dependent reflection contrast in near-zero-twist-angle WSe_2/WS_2 heterostructure.

8. Discussion on emerging features at higher energy

As shown in Fig. 2b in the text, the energy range near the WS_2 A exciton (2 ~ 2.2 eV) also shows richer resonance features than in the large-twist-angle case, which can potentially originate from moiré superlattice effect on WS_2 excitons. However, because the WSe_2 B exciton is in the same energy range, it is difficult to separate the responses from WSe_2 and WS_2 or make further quantitative analysis.

We note that the effective moiré potential on WS_2 and WSe_2 excitons is not necessarily symmetric and can be completely different. For example, Ref. 14 shows that the location of the moiré potential minimum for excitons in one layer can be the location of the potential maximum for excitons in the other layer. Therefore, the parameters used in our model to describe the effective moiré potential for WSe_2 excitons do not have direct implications on the effective potential for WS_2 excitons.

9. Dependence of moiré exciton absorption spectra on the moiré potential

The low-energy effective Hamiltonian of the A-exciton in monolayer WSe_2 is described by

$$H_0 = \left(E_0 + \frac{\hbar^2 \boldsymbol{Q}^2}{2M}\right)\tau_0 + J|\boldsymbol{Q}|\tau_0 + J|\boldsymbol{Q}|\left[\cos(2\phi_{\boldsymbol{Q}})\tau_x + \sin(2\phi_{\boldsymbol{Q}})\tau_y\right],$$

where $\boldsymbol{Q}$ is exciton total momentum, $\phi_{\boldsymbol{Q}}$ is the polar angle of $\boldsymbol{Q}$ in the momentum space, $M \approx m_0$ is the total mass of the electron and the hole, $J = 0.04\text{eV} \cdot \text{nm}$ describes the intra- and inter-valley exchange interaction, and τ_j $(j = 0, x, y, z)$ is the Pauli matrices for valley pseudospin[13]. Without the moiré potential, only the $\boldsymbol{Q} = 0$ exciton is bright due to the negligible momentum of photons, which has energy $E = E_0$.

With the moiré potential, the total Hamiltonian of the exciton becomes:

$$H = H_0 + V_m = H_0 + \sum_{j=1}^{6} V_j \exp(i\boldsymbol{b}_j \cdot \boldsymbol{r}).$$

When V is small (i.e. the "weak coupling" regime), the effect of the moiré potential can be intuitively understood from perturbation theory. The first order correction to the wavefunction dictates that states at $\boldsymbol{Q} = \boldsymbol{b}_j$ will be mixed with the $\boldsymbol{Q} = 0$ state in the following way:

$$\Phi(\boldsymbol{b}_j)^1 - \Phi(\boldsymbol{b}_j)^0 = \frac{\left\langle \Phi(\boldsymbol{b}_j)^0 \middle| V_m \middle| \Phi(0)^0 \right\rangle}{E(\boldsymbol{b}_j) - E_0}\Phi(0)^0 \sim \frac{V_j}{4E_m}\,\Phi(0)^0,$$

where $\Phi(\boldsymbol{Q})$ is the exciton center-of-mass wavefunction at momentum $\boldsymbol{Q}$ and $E_m = \hbar^2 b_j^2/(8M)$ is the exciton kinetic energy within the first mini-Brillouin zone. $E_m \sim 8$ meV in a WSe_2/WS_2 moiré superlattice with periodicity of ~ 8 nm. Because the wavefunction of excitons at $\boldsymbol{Q} = \boldsymbol{b}_j$ now contains part of the bright exciton wavefunction, their transition from the ground state is no longer completely forbidden and has oscillator strength $\sim\left|V_j/(4E_m)\right|^2 = [V/(4E_m)]^2$, giving an additional absorption peak at $4E_m = 30$ meV above the main peak. The magnitude of the moiré potential can therefore be obtained by examining the amplitude of this side peak in the absorption spectrum.

Figure S9a shows the simulated exciton absorption spectra with phase $\psi = 15°$ and different magnitudes of the moiré potential. The side peak amplitude shows a monotonic increase with larger V. The quantitative dependence deviates from the square scaling law at large V, which is expected since the perturbation treatment fails in the "strong-coupling" regime. By comparing

the experimental results to the simulation, we can extract the magnitude of the moiré potential to be $V \sim 25$ meV.

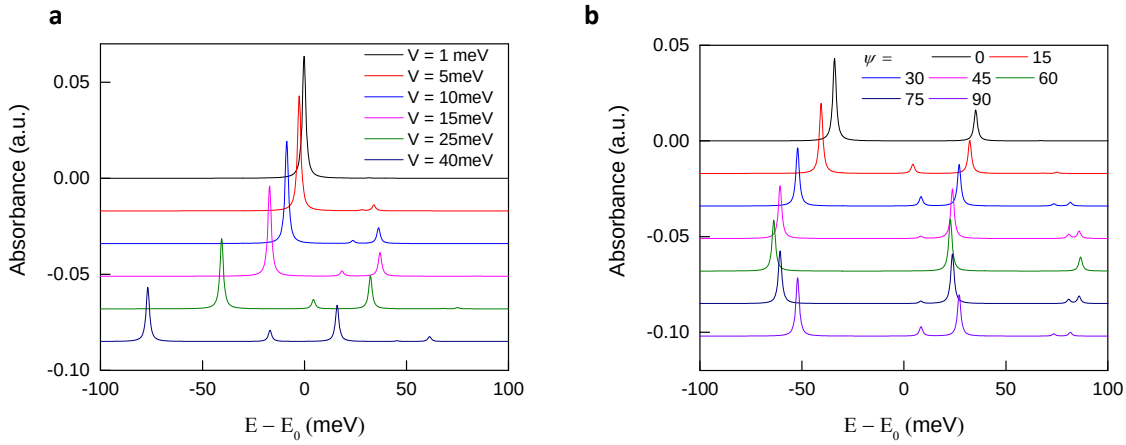

Fig. S9. **a**, Simulated exciton absorption spectra with different moiré potential magnitude V. $\psi = 15°$. **b**, Simulated exciton absorption spectra with different moiré potential phase ψ and $V = 25$ meV. Different curves are vertically shifted for visual clarity.

The phase ψ of the moiré potential plays a more subtle role: It has negligible effect on the absorption spectra in the "weak coupling" regime but will affect the spectra in the "strong coupling" regime, where higher order mixing between exciton states become important and different mixing paths start to interfere, as shown in Fig. S9b. The complicated dependence of the spectra on ψ makes it difficult to have an accurate determination through comparison to the experiment. However, different ψ will not qualitative change the properties of the system, e.g. between "weak coupling" regime and "strong coupling" regime.

10. Spatially localized exciton center-of-mass wavefunction

The general relation between the moiré potential and the above parameters is given by:

$$V_m = \sum_{j=1}^{6} V_j \exp(i\boldsymbol{b_j} \cdot \boldsymbol{r})$$

Where $V_1 = V_3 = V_5 = V\exp(i\psi)$ and $V_2 = V_4 = V_6 = V\exp(-i\psi)$. Therefore, the min-to-max value V_{pp} of the total moiré potential will depend on both V and ψ. Their quantitative relation is given by

$$V_{pp} = 12V \sin\left(\frac{\pi}{3}\right) \sin\left(\psi - \frac{2n\pi}{3} + \frac{\pi}{3}\right), \quad \psi \in \left[\frac{2n\pi}{3}, \frac{(2n+1)\pi}{3}\right)$$

$$V_{pp} = 12V \sin\left(\frac{\pi}{3}\right) \sin\left(\psi - \frac{2n\pi}{3}\right), \quad \psi \in \left[\frac{(2n+1)\pi}{3}, \frac{2(n+1)\pi}{3}\right)$$

where n is an integer. Figure S10 shows the real-space distribution of the moiré potential using the parameters $V = 25$ meV and $\psi = 15°$. After summing up the six components, the peak-to-peak amplitude of the moiré potential reaches ~ 250 meV, which is much larger than E_m. As a result, the lowest energy excitons are trapped around the potential minimum point (labelled as α), as discussed in the text.

We note that the exciton wavefunction discussed here refers to the center-of-mass envelop function for the 1s exciton state, which is spatially homogeneous without the moiré superlattice. This should not be confused with the relative motion between the electron and the hole within an exciton that defines atom-like levels, e.g. 1s and 2p states.

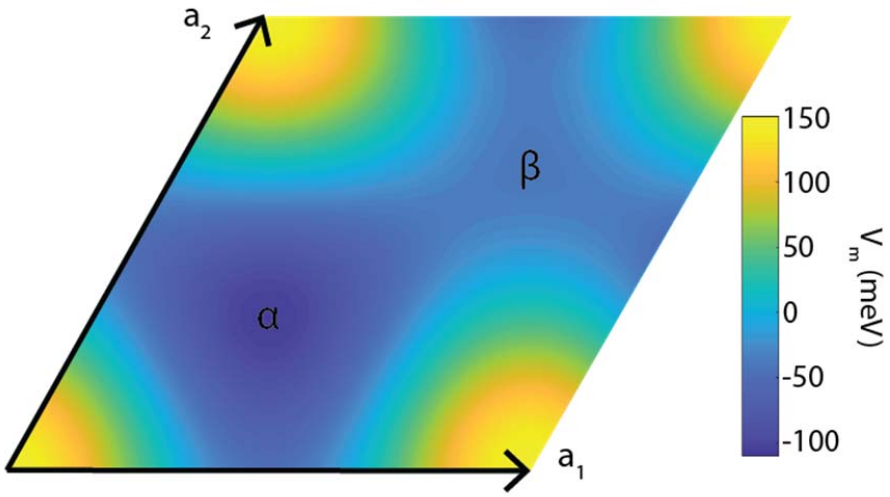

Fig. S10. Real space distribution of the moiré potential with $V = 25$ meV and $\psi = 15°$. The potential minimum is labelled as α.

11. Relation between the exciton band picture and localized exciton picture

The exciton band model described in the text can be alternatively calculated using a "tight-binding picture" parameterized by localized exciton orbitals at moiré potential minima and the inter-site hopping. Both approaches should yield the same correct Brillouin zone and band structure in a periodic system, regardless of the amplitude of the moiré potential.

In the tight binding model, the eigenstates are determined completely by the local orbitals at a single moiré superlattice site when the periodic potential is sufficiently large and the hopping

amplitude between the adjacent moiré sites is zero. In this case, the exciton band will be completely flat. For finite hopping amplitude between the adjacent moiré superlattice sites, there will be finite dispersion in the band structure. In the exciton moiré superlattices of WS_2/WSe_2 heterostructures, the hopping energy is in the order of few meV for the lowest exciton band and increases for the higher exciton bands. Although the hopping energy is smaller than the moiré superlattice potential, it is still significant and leads to the moiré exciton band structure that is described in the text.

12. Connection between the moiré potential to physical properties of the system

The value of the moiré potential at a given point in space can be approximately understood from the modulation of the local band structure by the interlayer interaction with local atom registry[13-15]. Therefore, its exact form will depend sensitively on the atomic configuration of the system, e.g. whether domain walls or lattice corrugations are formed. For example, one would expect the moiré potential to have a large amplitude if lattice corrugation exists because the interlayer interaction is extremely sensitive to the interlayer spacing.

However, it is very difficult to predict the atomic configuration in a given heterostructure and to make direct comparisons between moiré potentials in different heterostructures. For example, STM studies suggest that a significant lattice corrugation exists in WSe_2/MoS2 heterostructures[21,22]; while the DFT calculation in Ref. 13 uses two completely flat layers to model the $WSe_2/MoSe_2$ heterostructures. This can explain why the extracted moiré potential amplitude in the former case is orders of magnitude larger than the predicted values in the latter case. On the other hand, it is still unknown why the lattice forms corrugations in the WSe_2/MoS_2 case and whether corrugations also exist in the $WSe_2/MoSe_2$ case.

One would therefore expect that the moiré potential can be tuned dramatically by choosing different material combinations and relative alignments. Nevertheless, it is quite challenging to predict the parameters of the moiré potential for specific heterostructures unless the atomic configuration has been accurately determined. We hope that our work inspires future experimental work to understand the atomic reconstruction in a variety of heterostructures.

References:

32 Wang, F. *et al.* Gate-variable optical transitions in graphene. *Science* **320**, 206-209, (2008).

33 Jin, C. et al. Imaging of pure spin-valley diffusion current in WS_2-WSe_2 heterostructures. *Science* **360**, 893, (2018).